Resolving images by blurring: superresolution method with a scattering mask between the observed objects and the hologram recorder

Yuval Kashter,* A. Vijayakumar, and Joseph Rosen

Department of Electrical and Computer Engineering, Ben-Gurion University of the Negev, P.O. Box 653, Beer-Sheva 8410501, Israel
Corresponding author: kashter@post.bgu.ac.il

An important quest in optical imaging has been, and still is, extending the resolution of imaging systems beyond the diffraction limit. We propose a superresolution technique in which the image is first blurred by a scattering mask, and then recovered from the blurry data with improved resolution. We introduced a scattering mask into the space between the observed objects and the objective lens of a Fresnel incoherent correlation holography (FINCH) system to demonstrate the method. Optical waves, containing high spatial frequencies of the object, which are usually filtered out by the limited system aperture, were introduced into the system due to the scattering nature of the scattering mask. As a consequence, both the effective numerical aperture and the spatial bandwidth of the system were enlarged. The image resolution could therefore be improved far beyond the resolution limit dictated by the limited numerical aperture of the system. We demonstrated the technique using a modified FINCH system and the results were compared with other systems, all having the same aperture dimensions. We showed a resolution enhancement in comparison to conventional FINCH and regular imaging systems, with the same numerical apertures. The theoretical and experimental data presented here establishes the proposed method as an attractive platform for an advanced superresolution system that can resolve better than conventional imaging systems. © 2017 Optical Society of America

1. INTRODUCTION

Imaging is the technique of recording a visual representation of an object [1–4]. One of the important goals in imaging is to be able to resolve as small as possible visual details of the object. However, in optical imaging, the barrier in achieving this goal is the diffraction limit i.e., the inability to collect all of the light diffracted from the object due to the limited aperture size of the imaging system [5]. Different techniques have been developed to surpass the diffraction limit [6–13]. These methods usually gain the resolving power at the expense of either the field of view (FOV) or the time resolution. In other words, either the resolving power is gained only in a relatively small area out of the entire object area [7], or relatively many images of the same object, under different conditions, are acquired over time [8–13].

Holography is an indirect method of imaging that provides the ability to record and reconstruct 3D information of an object [14]. An incoherent digital holography technique termed Fresnel incoherent correlation holography (FINCH) was invented in 2007 [15–17]. FINCH has been proved to resolve images better than a non-holographic lens-based imaging system with the same numerical aperture (NA) [17]. This peculiarity of FINCH arises due to its operation mode of recording holograms by a self-interference. Hence, FINCH breaks the classical limits governed by the Lagrange invariant condition [18] and enables, under specific conditions [17,18], resolution beyond the diffraction limit by theoretical factors of 2 and 1.5, in comparison with conventional coherent and incoherent systems with the same NA, respectively. Recently, an optical configuration of FINCH with structured illumination was demonstrated to resolve images beyond the resolution limit of FINCH dictated by the NA of the system [19].

In this study, we propose a new technique to gain the resolving power of the FINCH system beyond the diffraction resolution limit. In the proposed technique, a random-like coded phase mask (CPM) is introduced between the object and the FINCH system. The CPM, when displayed in front of the object, diffuses part of the incident light into the system, including the high spatial frequencies that are otherwise discarded by the system due to its limited NA. By capturing the otherwise-lost high spatial frequencies, the effective NA is increased beyond the physical NA of the system. Consequently, the effective spatial bandwidth of the system is enlarged, and smaller details of the object can be resolved. Since the proposed method is FINCH enhanced by the CPM, it is dubbed coded FINCH (C-FINCH).

Although resolution enhancement of FINCH is demonstrated herein, the current methods of hologram recording and reconstruction are similar to another technique of incoherent hologram recording, known by the term coded aperture correlation holography (COACH) [20]. Like FINCH, COACH can be classified as an incoherent self-reference holography system in which the beam radiated from the object is split into two beams. One of these beams passes through a CPM displayed on a spatial light modulator (SLM). From the SLM, the beam propagates to the sensor plane on which it interferes with another beam that comes from the same object but without being modulated by the CPM. The intensity distribution of the two-beam interference is stored in the computer as a digital hologram. At least two holograms must be recorded in this method. Before recording the hologram of an object, one should record at least one point spread hologram (PSH). The PSH is a hologram of a point source located in the center of the plane on which the object is displayed. Both the PSH and the object hologram are recorded under the same conditions and with the same CPM. The PSH is used in the digital reconstruction stage, such that the image is digitally reconstructed by correlating the object hologram with the PSH. These techniques of recording and reconstruction are also applied in the present C-FINCH method for superresolution.

There is also some similarity between C-FINCH and Kim's work on imaging with an incoherent self-reference holography system through a scattering medium [21,22]. However, unlike Refs. [21,22] where the scattering medium is a given unchangeable disturbing element, in C-FINCH, the scattering medium is artificially synthesized and controllably changed, not only to image the object covered by this scattering medium but also to resolve the image with better image resolution than in the case without the scattering medium.

Another pioneer study that employs a random pattern to achieve superresolution is the turbid lens imaging (TLI) technique proposed by Choi et al. [23,24]. In TLI, the effective NA is increased, and thus the image resolution is improved due to scattering of waves with high spatial frequencies by the turbid media. The purpose of the CPM presented in our study is similar to the turbid media. However, TLI and C-FINCH are different in almost any other aspect. TLI operates only with coherent light, whereas C-FINCH works only with incoherent light. Additionally, the training process of the system and the reconstruction procedure are different, and apparently more efficient, in C-FINCH. Because of the use of incoherent light, the C-FINCH technique can be applied for fluorescence and other incoherent microscopy techniques. Moreover, unlike [23,24], in this study, we have investigated the behavior of C-FINCH under different degrees of scattering.

The advantages of the proposed method are: (1) A resolution enhancement of more than triple is achieved in the present experiment, but theoretically the system aperture can stop being a limiting factor of the image resolution. (2) Relatively short time of image acquisition is employed. (3) The imaging system is passive without emitting any signal or radiation toward the object, and it operates well with any kind of incoherent illumination (e.g., fluorescent illumination). (4) The process of capturing the images is completely motionless, performed from a single viewpoint and without any scanning. (5) The method can be applied to any imaging application that can be implemented by a FINCH system or by any other self-interference hologram recorder. (6) The resolution enhancement is controllable such that a user can adjust

electronically between the parameters of resolving power versus the size of the FOV.

The paper consists of four sections. In the second section, the methodology of this study is presented. The experimental procedure is discussed in the third section. The comparison results of the proposed technique with regular imaging and FINCH are presented in the final section. In addition, detailed analysis of the geometry of C-FINCH is presented in Appendix A.

2. METHODOLOGY

The scheme illustrated in Fig. 1(a) describes the optical configuration of the C-FINCH. A pinhole is critically illuminated [25] by a spatially incoherent and quasi-monochromatic light source using the lens L_0. Thus, light diffracted from every point on the object plane can interfere only with itself, and it cannot interfere with light diffracted from a different point, enabling the implementation of the self-interference principle. The light emitted from an object point is incident on the CPM located at a distance of d_1 from the object plane. The CPM is computed by the Gerchberg–Saxton algorithm (GSA) [26], illustrated in Fig. 2. For every iteration, two constraints are defined in the spatial and frequency domains. In the CPM domain, the complex amplitude is constrained to be a pure phase because the CPM is a pure phase mask. In the spectrum domain, the constraint is such that the complex amplitude should have a uniform magnitude over the desired area of the spatial spectrum with the bandwidth of $2B = 2B_x = 2B_y$. This bandwidth controls the degree of scattering of the CPM. When B is maximal, the CPM scatters the incident light along all the possible angles up to the angle $\pm\lambda/2\Delta$, where λ is the central wavelength of the illumination,
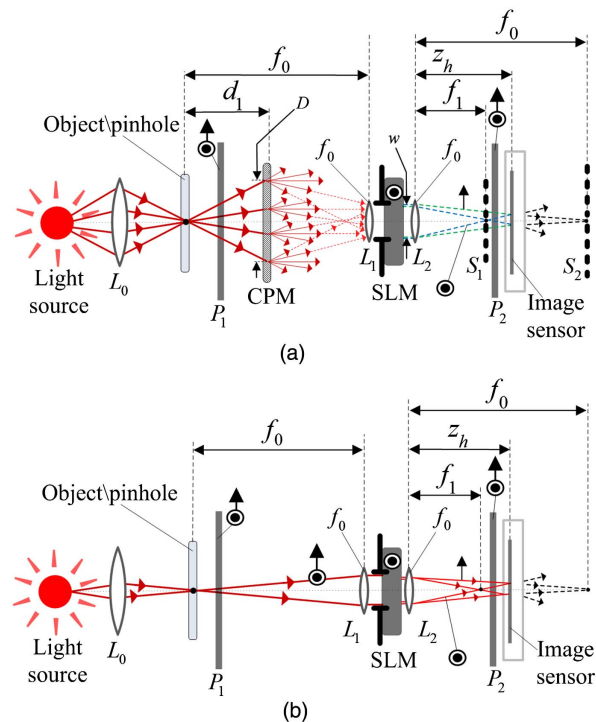

Fig. 1. Optical schemes of (a) C-FINCH system and (b) dual lens FINCH system. P_1 and P_2, polarizers; L_o, objective lens; L_1 and L_2, converging lenses; CPM, coded phase mask, SLM, spatial light modulator.
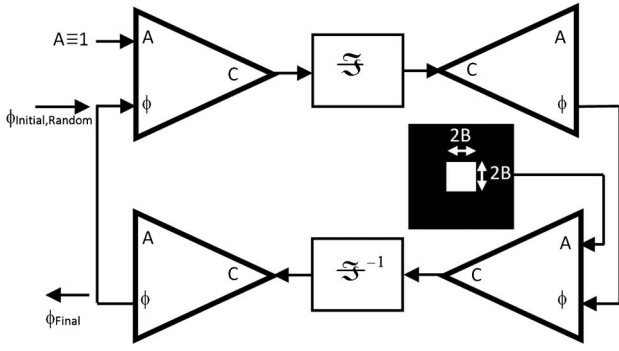
Fig. 2. Block diagram illustrates the GSA. $\mathfrak{F}$ and $\mathfrak{F}^{-1}$ represent forward and backward Fourier transforms, respectively. A, ϕ, and C represent magnitude, phase, and complex matrices, respectively.

and Δ is the pixel size of the CPM. We define the ratio $\sigma = B/B_{max}$ (where $2B_{max}$ is the maximal spectral bandwidth) as the scattering degree, which is a value that can be varied between 0 and 1. It is shown later that the scattering degree σ controls the trade-off between the resolution enhancement and the FOV size. The CPM on which a pure random phase (after n iterations of the GSA) is produced with an effective diameter D diffuses the incident light and acquires the high frequencies that are otherwise discarded by the limited NA of the system. The effective diameter is the diameter of the part of the CPM that participates in the imaging process, i.e., the light scattered from this part is introduced into the FINCH section of the system and recorded by the camera. A refractive lens L_1 is mounted at a distance of f_0 from the object plane to collect the light diffused by the CPM and projects the beams onto an SLM located right behind L_1. The polarization of the light diffracted by the pinhole is oriented at 45° with respect to the active axis of the SLM using a polarizer P_1. On the SLM, a diffractive lens with a focal length of f_d is displayed. Since the SLM active axis is oriented at 45° with respect to the polarization of the incident light, two optical channels are created corresponding to the two orthogonal polarization directions. Hence, the SLM is employed as a beam splitter of two orthogonal polarization orientations. A refractive lens L_2 with a focal distance of f_o is located behind the SLM, implementing the dual lens FINCH configuration [27].

Unlike regular dual lens FINCH, the two spherical waves propagating beyond L_2 in C-FINCH are distorted due to the scattering nature of the CPM. The two scattered waves propagate to distances of f_0 and f_1 from the lens L_2 and create two scattered images. A second polarizer P_2 oriented at an angle of 45°, with respect to the active axis of the SLM, enables interference between the two scattered waves. An image sensor located at a distance of z_h from L_2 is used to record the hologram. The bias terms and the twin image are canceled from the hologram using the phase shift method, similar to [15]. This phase-shift process involves displaying three diffractive lenses, each with a focal length f_d but with three phase constants of $\theta_{1,2,3} = 0, 2\pi/3$, and $4\pi/3$. The three recorded raw holograms are stored in the computer and are superposed according to Eq. (2). Consequently, a complex hologram of the point object, denoted as H_{PSH}, is obtained.

The hologram acquisition is repeated for the object, with the same system arrangement and the same CPM as in the case of H_{PSH}, by replacing the pinhole by the object exactly at the same

axial location. Three holograms are recorded again corresponding to the three phase masks displayed on the SLM, and the complex hologram resulting from their superposition is denoted H_{OBJ}. The image of the object is reconstructed by cross-correlating H_{OBJ} with a phase-only filtered version of H_{PSH} in order to improve the signal-to-noise ratio (SNR) [28]. Note that it is sufficient to record the H_{PSH} only once as part of the training of the system, and the same H_{PSH} can be used to reconstruct an unlimited number of object holograms (located at the same axial distance).

Next, we describe the process of the hologram acquisition and reconstruction more rigorously in order to evaluate the various parameters of the imaging. As mentioned, there are two optical elements displayed on the SLM corresponding to the two different linear polarizations: a diffractive lens with a focal length f_d, and a constant phase. Therefore, in the absence of the CPM [see Fig. 1(b)], there are two imaging systems in the same optical channel corresponding to the two orthogonal polarizations. The images of the object are obtained at two different planes, S_1 and S_2, at the respective distances of f_0 and $f_1 = 1/[1/f_d + 1/f_0]$ from the lens L_2. The camera plane is located between S_1 and S_2, such that there is a perfect overlap between the interfering beams on the camera plane. As explained in Ref. [27], this condition of beam overlap guarantees maximum resolving power in the case of classical FINCH. Although this condition is not valid for C-FINCH, we fulfill this condition to compare the imaging results of C-FINCH with that of optimal FINCH. The overlap condition imposes that the distance between the lens L_2 and the camera is, $z_h = 2f_o f_1/(f_o + f_1)$.

When the CPM is introduced into the system [Fig. 1(a)] at a distance of d_1 from the object plane, and the system is illuminated from the object plane by a single point located at (x_s, y_s) with the amplitude of $\sqrt{I_j}$, the two image planes of the point object (without the CPM) become the Fourier planes of the CPM [14]. Moreover, the centers of these Fourier distributions are located at the images of the point object. In other words, on plane S_1, around the point $(-x_s, -y_s)f_1/f_o$, there is a Fourier transform of the CPM (multiplied by a quadratic phase function) with a diameter of about $\lambda d_1 \sigma f_1/(f_o\Delta)$. On plane S_2, around the point $(-x_s, -y_s)$, there is another Fourier transform of the CPM (multiplied by a different quadratic phase function) but with a diameter of about $\lambda d_1 \sigma/\Delta$. The camera is placed between the planes S_1 and S_2, a relatively short distance from both of them. Therefore, based on geometrical considerations, we can assume that on the camera plane, beyond the polarizer P_2, there is a sum of two distributions; both are centered on the point $(U, V) = (-x_s, -y_s)z_h/f_o$, and both have the same diameter of about $D_I = \lambda d_1 \sigma z_h/(f_o\Delta)$. Thus, the intensity distribution recoded by the camera is

$$I(u,v;\theta_i) = \left| \sqrt{I_j} G_1\left(\frac{u-U, v-V}{D_I}\right) + \sqrt{I_j} G_2\left(\frac{u-U, v-V}{D_I}\right) \right|^2,$$
(1)

where G_1 and G_2 are the complex amplitudes on the camera plane. G_1 propagates from plane S_1 to the camera plane, and G_2 propagates (virtually) from the camera plane and becomes the Fourier distribution on plane S_2. A complex digital hologram of any point located at (x_s, y_s) is synthesized from three intensity recordings with phase shifts $\theta_{1,2,3} = 0, 2\pi/3$, and $4\pi/3$ according to the following equation,

$$H_{p,j}(u,v) = I(u,v;\theta_1)[\exp(-i\theta_3) - \exp(-i\theta_2)]$$
$$+ I(u,v;\theta_2)[\exp(-i\theta_1) - \exp(-i\theta_3)]$$
$$+ I(u,v;\theta_3)[\exp(-i\theta_2) - \exp(-i\theta_1)], \quad (2)$$

in order to remove the twin image and the bias terms during reconstruction. Finally, the synthesized complex digital hologram of the point at (x_s, y_s) is

$$H_{P,j}(u-U, v-V) = I_j \cdot G_1\left(\frac{u-U, v-V}{D_I}\right) G_2^*\left(\frac{u-U, v-V}{D_I}\right). \quad (3)$$

An arbitrary object composed of multiple incoherent source points is given by

$$I_s(x,y) = \sum_j I_j \delta(x - x_{s,j}, y - y_{s,j}). \quad (4)$$

The complex hologram of the multiple-points object is a superposition of the point holograms, as the following:

$$H_{\mathrm{OBJ}}(u,v) = \sum_j H_{P,j}(u - U_j, v - V_j). \quad (5)$$

In order to reconstruct the image from the hologram, we use the PSH given by

$$H_{\mathrm{PSH}}(u,v) = G_1\left(\frac{u,v}{D_I}\right) G_2^*\left(\frac{u,v}{D_I}\right). \quad (6)$$

This PSH is Fourier transformed, and only its phase profile is extracted and used in the process of the digital spatial filtering. The reconstructed image of the object is obtained as a correlation of H_{OBJ}, with the inverse Fourier transform of the phase profile of H_{PSH}, as the following:

$$T(x,y) = \iint H_{\mathrm{OBJ}}(u,v) \tilde{H}_{\mathrm{PSH}}^*(u-x, v-y) \mathrm{d}u\mathrm{d}v$$
$$= \iint \sum_j H_{P,j}(u - U_j, u - V_j) \tilde{H}_{\mathrm{PSH}}^*(u-x, v-y) \mathrm{d}u\mathrm{d}v$$
$$\approx \sum_j I_j \Lambda(x - U_j, y - V_j) = I_s\left(\frac{f_o}{z_h}(x,y)\right), \quad (7)$$

where $\tilde{H}_{\mathrm{PSH}}(u,v) = \mathfrak{F}^{-1}\{\exp[i \cdot \arg(\mathfrak{F}\{H_{\mathrm{PSH}}(u,v)\})]\}$, and where $\mathfrak{F}$ and $\mathfrak{F}^{-1}$ stand for 2D Fourier and inverse Fourier transforms, respectively. Λ in Eq. (7) is a δ-like function, approximately equal to 1 around $(0,0)$ and to small negligible values elsewhere. Λ is the result of the cross-correlation between H_{PSH} and $\tilde{H}_{\mathrm{PSH}}(u,v)$. It is evident from Eq. (7) that because the object hologram is an incoherent sum of point responses, each of which is located at $(U_j, V_j) = (-x_{s,j}, -y_{s,j})z_h/f_o$, then a cross-correlation with $\tilde{H}_{\mathrm{PSH}}(u,v)$ yields a collection of δ-like functions, which together create the magnified image.

Few imaging properties can be deduced from this analysis. Equation (7) indicates that the lateral magnification of C-FINCH is $M_T = z_h/f_o$. The minimum resolved size on the image plane is the correlation length of the cross-correlation of Eq. (7), which is given by the smallest element that can be created on the camera plane. This smallest feature size cannot be deduced directly from Eq. (7) but is estimated by the following reasoning. Since planes S_1 and S_2 are in Fourier relations with the CPM, with the scaling factors of λd_1 and $\lambda d_1 f_1/f_o$, respectively, the relation between the camera plane and the CPM can be

approximated to a Fourier relation with the scaling factor of $\lambda d_1 z_h/f_o$. For an effective diameter of the CPM of D, the smallest feature size that can be measured on the camera plane has the size of $\lambda d_1 z_h/(D f_o) = M_T \lambda/(2 \tan \theta_m)$, where θ_m is the maximal diffraction angle of the central point object recorded by the camera (see Appendix A). Therefore, the minimum resolvable size on the object plane is $\lambda/(2 \tan \theta_m)$. This result confirms that the CPM extends the effective NA of the C-FINCH by scattering light into the system, which is otherwise discarded by the limited aperture size of the FINCH system. The maximal diffraction angle θ_m of the central source point recorded by the camera is given in Appendix A by Eq. (A1) as follows,

$$\sin\theta_m = \begin{cases} \frac{\lambda\sigma}{2f_0\Delta}(f_0 - d_1) + \frac{w}{2f_0} & D \geq \gamma \\ \frac{D}{2d_1} & D < \gamma \end{cases}, \quad (8)$$

where γ is given by Eq. (A3) and w is the diameter of the input aperture of the FINCH system. As expected, the effective NA (NA $= \sin\theta_m$) is increased (from an initial NA of the classical FINCH of $w/2f_0$) with a higher scattering degree σ. It should also be noted that a small ratio of d_1/f_o also enlarges the effective NA and thus improves the imaging resolution, but this benefit is achieved at the expense of the power efficiency of the imaging.

Another important feature of imaging is the FOV. Assuming the FOV in the object domain without the presence of the CPM has dimensions of $V_0 \times V_0$, then on the camera, taking into consideration the magnification factor, the FOV has dimensions of $M_T(V_0 \times V_0)$. As the intensity distribution of any point source increases at the camera plane with the increase of the degree of scattering, the area of the hologram becomes larger than that of the regular FINCH. The increment in the area of the hologram is additive since, according to Eq. (5), the C-FINCH hologram is a convolution of H_{PSH} with the image, without the CPM, at the camera plane. Therefore, the size of the C-FINCH hologram is the sum of the FINCH hologram with the size of H_{PSH}. Consequently, from the FOV of FINCH, one should subtract the size of H_{PSH} projected to the object plane. As mentioned, when the CPM is illuminated by a point source from the object plane, the dimensions of the intensity distribution on the camera are about $D_I \times D_I$, where $D_I = \lambda d_1 \sigma z_h/(f_o\Delta)$. Therefore, the FOV size of C-FINCH at the object plane is $V_c \times V_c$, where

$$V_c = V_0 - \frac{\lambda d_1 \sigma z_h}{f_o \Delta M_T} = V_0 - \frac{\lambda d_1 \sigma}{\Delta}. \quad (9)$$

From this expression, it is clear that as the scattering degree σ is increased, the resolution of C-FINCH is enhanced at the expense of the FOV size. Note that decreasing the distance d_1 increases both resolving power and the FOV, but as mentioned, there is still a problem of power loss when the scattering by the CPM is too far from the FINCH system.

3. EXPERIMENTAL PROCEDURE

To demonstrate the resolution capabilities of C-FINCH and to compare its performance with that of FINCH and regular imaging, the experimental setup shown in Fig. 3 was constructed with the ability to switch electronically between the various imaging systems without altering the setup and without any mechanical movements. Two identical lasers (Helium–Neon lasers $\lambda = 632.8$ nm), denoted as LS_1 and LS_2, were spatially filtered by two spatial filter modules, SF_1 and SF_2, respectively. The back
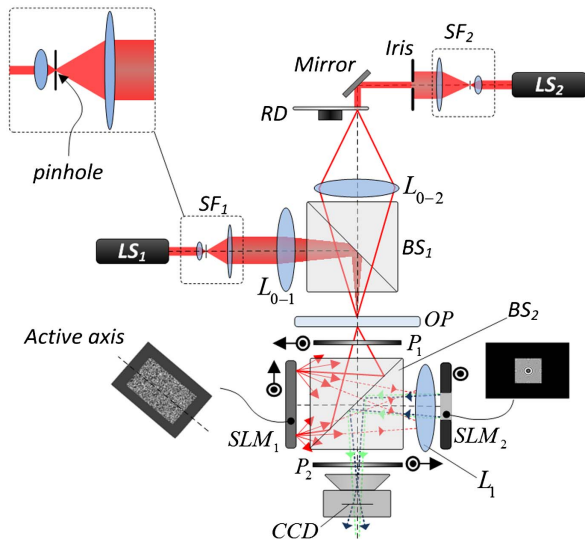
Fig. 3. Experimental setup of C-FINCH: LS_1 and LS_2, laser sources, SF_1 and SF_2, spatial filters; BS_1 and BS_2, beam splitters; P_1 and P_2, polarizers; L_{0-1} and L_{0-2}, objective lenses; L_1, converging lens; SLM_1 and SLM_2, spatial light modulators; CCD, charge-coupled device; RD, rotating diffuser.

focal plane of the lens L_{0-1} is located on the object plane (OP), so that the pinhole of SF_1 is imaged on the OP to ensure the same axial distance for both the object and the pinhole. By this way, the first channel illuminated by LS_1 is employed as the PSH channel, and the second channel illuminated by LS_2 is employed as the object channel. The light emitted by LS_2 is converted to a spatially incoherent source by transmitting the light through a rotating diffuser denoted as RD. The lens L_{0-2} is used to project the source on the object in a mode of critical illumination. The Iris located in front of SF_2 controls the size of the illuminated area on the OP, according to the required FOV. The beam splitter BS_1 is used to combine the light from the two illumination channels. A negative resolution chart (1951 USAF resolution test chart) is mounted at the OP, and the pinhole (5 μm in diameter) is imaged on it from channel 1. The pinhole is imaged on the center of the observed region on the object. The light from the pinhole is transferred into the system through a transparent region of the chart. Beyond the OP the light is polarized by a polarizer P_1 oriented at 45° with respect to the active axis of SLM_2. From P_1, the light is reflected by a beam splitter BS_2 on a phase only SLM_1 (Holoeye PLUTO, 1920 × 1080 pixels, 8 μm pixel pitch, phase-only modulation) employed as the CPM, which is located at an axial distance of $d_1 = 125$ mm from the OP. SLM_1 is also rotated by 45° with respect to SLM_2 so that its active axis is collinear with the incident polarized light. By doing so, maximum modulation of the incident light is guaranteed. Using SLM_1 for displaying CPM allows electronic control of the CPM produced by the mentioned GSA. The light modulated by the CPM is incident, through the lens L_1 on SLM_2 (same as SLM_1), on which the three diffractive lenses ($f_d = 520$ mm) with three different phase shift values, $\theta = 0, 2\pi/3$, and $4\pi/3$, are displayed. The refractive lens L_1 ($f_0 = 250$ mm) implements both lenses L_1 and L_2 of Fig. 1. As a result, the light scattered by SLM_1 is collected by L_1 mounted close to SLM_2 in order to transfer maximum scattered light to SLM_2. As a result, the modulated beam

converges to the distance $f_1 = 168.8$ mm from the lens L_1. The system aperture is determined by the diffractive lens displayed on SLM_2, which is limited in the present experiment by a rectangular mask of 280 × 280 pixels (2.24 × 2.24 mm). From SLM_2 the light is reflected by BS_2 and meets a second polarizer P_2, oriented at 45° with respect to the active axis of SLM_2. Because of the orientation of P_2, the modulated and unmodulated beams reflected by SLM_2 can interfere with each other. The image sensor (GigE vision GT Prosilica, 2750 × 2200 pixels, 4.54 μm pixel pitch) located at the hologram plane at a distance of $z_h = 201.6$ mm from SLM_2 (determined according to the mentioned overlap condition) records the holograms. The polarization direction of P_2 is perpendicular to the orientation of P_1, and therefore the incident light arriving directly through BS_2 from the OP is blocked. The holograms of the pinhole and the object were recorded for the three phase shift values and superposed according to Ref. [15] to create complex holograms for the object and the pinhole.

The space between adjacent pixels and the fill factor of SLM_1 yields a relatively intense unscattered beam, reducing the effect of the scattered light. To cancel the effect of the unscattered beam, the same two CPMs were displayed on SLM_1 with phase shifts of $\varphi = 0, \pi$, and the resulting holograms are superposed. As a result, six exposures in total are needed for recording each of the object and the pinhole complex holograms. To improve the SNR of the reconstructed image and to reduce the effects of other noise sources (e.g., stray light, CCD noise), five sets of holograms were recorded for both the pinhole and the object with five different independent CPMs. The resulting five complex reconstructed images from the correlation of the corresponding $H_{PSH}s$ and $H_{OBJ}s$ were averaged to improve the SNR [28].

The same setup in Fig. 3 is used to implement the conventional FINCH and the regular imaging systems for the purpose of comparison with C-FINCH. Switching between the various systems is done electronically by displaying various phase masks on the SLMs as the following: in the case of the conventional FINCH, SLM_1 is inactivated and hence is considered as a constant phase plate. To implement a regular imaging system, SLM_1 is operated as a planar mirror, and a diffractive lens satisfying the imaging condition from the object to the CCD planes is displayed on SLM_2.

4. RESULTS AND DISCUSSION

The comparison results of C-FINCH for different values of σ, regular FINCH, and regular imaging are shown in Fig. 4. To demonstrate the resolution enhancement, two different experiments were conducted, each with a different purpose. In the first experiment, the resolution enhancement in C-FINCH was studied by analyzing the improvement in the visibility of the reconstructed images for various scattering degrees, as shown in Figs. 4(a1)–4(a9) and 4(b1)–4(b9). In the second experiment, we looked for the smallest lines on the chart that can be still resolved for each value of the scattering degree σ. It can be noted that in the case where $\sigma = 0$, the imaging is actually done by a regular FINCH. Figures 4(a1)–4(a9) demonstrate the increase of visibility due to the improvement in the resolution. The graphs presented in Figs. 4(b1)–4(b9) show the intensity profile along the dashed red lines of Figs. 4(a1)–4(a9). Figures 4(c2)–4(c9) and 4(d2)–4(d9) show the smallest lines that can be resolved

and the magnitude of the complex PSH, for various scattering degrees, respectively.

Visibility is used as a measure of resolution according to the Rayleigh resolution criterion in which the capability to resolve two points is dependent on the visibility of the two-point image, i.e., the ratio of the difference between the peak and the valley (between the points of the image) and the sum of the peak and the valley. It is evident from the visibility plots that the resolution of the C-FINCH is better than FINCH and regular imaging. It can also be noted that with the increase in the scattering degree, the resolution is improved. However, as expected, with a gradual increase in the resolution, there is a gradual loss of FOV. Thus, C-FINCH is a superresolution method that enhances the resolution more with the increase of the scattering degree of the CPM, at the expense of the FOV size reduction. Figure 5(a) presents the plot of the visibility values measured from Figs. 4(b2)–4(b9) versus the eight different values of the scattering degree.

In the second experiment, we investigate the smallest resolvable element in the case of the eight scattering degrees. Thus, the spatial bandwidth increase can be estimated. Figure 5(b) presents
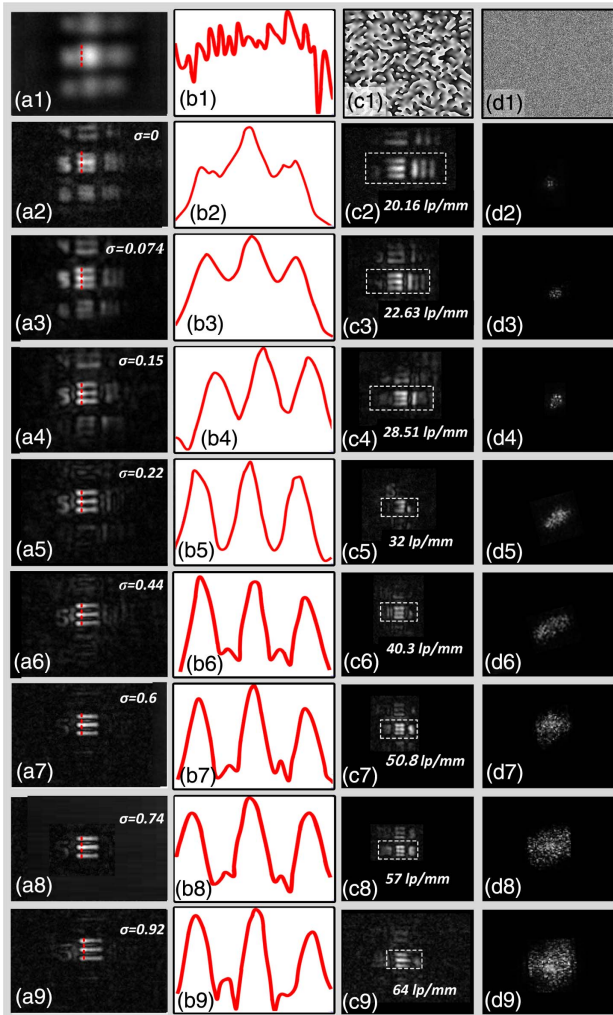
a comparative graph of the cutoff frequency ν_c calculated theoretically by $\sin\theta_m/\lambda$, where $\sin\theta_m$ is given by Eq. (A1) (presented as the dash linear graph), where all the distances in Eq. (A1) have been corrected for the path through the BS$_2$. The experimental measurements from Figs. 4(c2)–4(c9) are presented in Fig. 5(b) by the blue rings.

As mentioned, to improve the SNR of the final images presented in Fig. 4, five complex reconstructed images corresponding to five different uncorrelated CPMs were averaged. To estimate the SNR improvement, an object in the form of a square is selected. FINCH and C-FINCH (with scattering degree of 0.44) were implemented, and the SNR of a single reconstruction and average of five complex reconstructions were calculated as shown in Fig. 6. This averaging technique is only a tool to enhance the SNR and is not a strict requirement of the C-FINCH technique.

C-FINCH is different from other diffraction-limited superresolution methods [8–13] in the sense that to improve the resolution, it does not acquire more visual information of the same scene. The spatial bandwidth of the image is enlarged, but a single acquired hologram contains the entire enlarged spatial spectrum of the object. Therefore, the overall information amount of C-FINCH is identical to that of FINCH with the same aperture size. The space-bandwidth product (SBP) is known as a measure of information quantity. Because C-FINCH acquires a single complex hologram with the same FINCH setup, the SBP of both systems is identical. Since it is evident theoretically and experimentally that the system bandwidth of C-FINCH is larger than of FINCH, the FOV size ("S" in the SBP) of C-FINCH must be smaller, as has indeed been demonstrated both theoretically and experimentally herein.

Working with a programmable SLM with a variable degree of scattering enables one to make the trade-off between the image resolution and the FOV. However, the current technology of
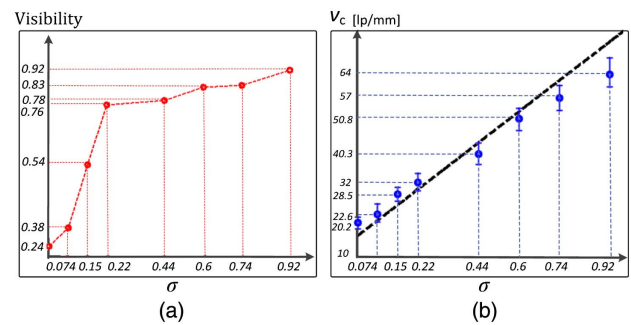

Fig. 4. Comparison results of C-FINCH with FINCH and regular imaging. (a1)–(a9) The reconstructed images of 25.4 lp/mm. (b1)–(b9) Intensity cross-sections. (c1) CPM with $\sigma = 0.074$. (d1) CPM with $\sigma = 0.92$. (c2)–(c9) The smallest resolvable element. (d2)–(d9) The magnitude of PSH.

Fig. 5. Resolution improvement graphs. (a) Visibility versus the scattering degree, corresponding to Figs. 4(b2)–4(b9). (b) Cutoff frequency versus the scattering degree corresponding to Figs. 4(c2)–4(c9).
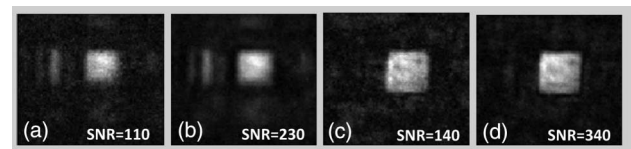

Fig. 6. SNR results of C-FINCH and FINCH. (a) Single reconstructed image of FINCH. (b) Average of five complex reconstructions of FINCH. (c) Single reconstructed image of C-FINCH. (d) Average of five complex reconstructions of C-FINCH.

SLMs with 8 μm pixel size (and a relatively limited effective area of 8.19×15.4 mm) does not enable implementation of C-FINCH in microscopes due to the relatively low scattering angle. Nevertheless, the experiments presented in Refs. [23,24] prove that microscopic scattering layers between the specimen and the microscope objective can improve the image resolution of the microscope.

Like COACH [20,28], the present C-FINCH can be extended to 3D imaging by creating a library of PSHs, i.e., a set of digital holograms of a single point located on the optical axis at different Z distances from the imaging system. An object hologram of a multi-plane object can be reconstructed plane by plane using different pre-recorded PSHs from the library. Figure 7 presents an example of 3D imaging implemented using C-FINCH. Four reconstructed images were recorded by the C-FINCH with a scattering degree of 0.22, whereas the mentioned resolution chart was located in two different planes. Plane 1 and Plane 2 are located at 250 and 245 mm from the lens L_1, respectively. By using the setup presented in Fig. 3, the object and the pinhole are shifted along the axial direction by 5 mm. Two holograms and two PSHs were recorded in the two mentioned axial locations. Only when the object holograms are correlated with the appropriate PSH recorded at the same axial distance is a relatively high quality reconstructed image obtained. In case the object hologram is correlated with a different PSH recorded at a different axial distance, the reconstruction is blurred due to the relatively short axial correlation length. Hence, according to this result, we can conclude that C-FINCH has the capability of 3D imaging. For reconstructing images of 3D objects at different axial planes, a library of pre-recorded PSHs should be prepared *a priori*. However, this PSH library needs to be created only once and can be used any number of times to reconstruct the images of any objects. Other feature of C-FINCH that has not been dealt with in the present study but that is expected to provide an
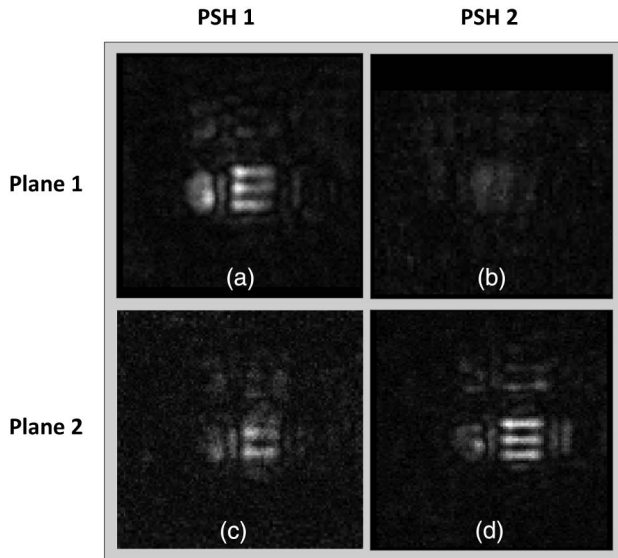

Fig. 7. Results of C-FINCH with two object planes. (a) Reconstruction of the hologram given at plane 1 with PSH recorded at plane 1. (b) Reconstruction of the hologram given at plane 1 with PSH recorded at plane 2. (c) Reconstruction of the hologram given at plane 2 with PSH recorded at plane 1. (d) Reconstruction of the hologram given at plane 2 with PSH recorded at plane 2.

additional benefit is the improved axial resolution. This benefit is expected based on our studies of COACH [20,28] and will be investigated in the future.

APPENDIX A

In this appendix, marginal ray tracing analysis is discussed to understand the performance of C-FINCH with respect to regular FINCH and regular imaging. Figure 8 shows the marginal ray tracing in the presence (solid lines) and absence (dashed lines) of CPM. It seems that in the presence of CPM, light rays (solid lines) emerging with larger angles of diffraction are collected by the system aperture in comparison with the case without the CPM. All the following analysis is done under the assumption of small angles.

The angle θ_σ represents the angle between the marginal ray that meets the CPM and the diffracted ray that enters into the system aperture due to scattering and is dictated by the spectral bandwidth $2B$ that is chosen in the GSA process as follows: $\theta_\sigma = \lambda \cdot B$. From the geometry of the setup, the maximal angle diffracted from the object and still acquired by the system (denoted as θ_m in Fig. 8) is given as: $\theta_m = \tan^{-1}[(2(f_0 - d_1) \tan(\theta_\sigma - \theta_m) + w)/2d_1]$.

Taking into consideration that $w \ll f_0$, the angle of the marginal ray can be simplified as

$$\sin \theta_m = \frac{\frac{\lambda \sigma}{\Delta}(f_0 - d_1) + w}{2f_0}. \tag{A1}$$

In the special case, where the cutoff frequency and the scattering degree are zero, the angle θ_m is reduced to θ_0, representing the NA of a classical FINCH system. Therefore, the gain of the NA, η, can be equally expressed by the ratio between θ_m and θ_0, as

$$\eta = \frac{\lambda \sigma(f_0 - d_1)}{w\Delta} + 1. \tag{A2}$$

In the result of Eq. (A1), it is assumed that the CPM is large enough that the effective NA is not dependent on the CPM size. However, in the case where the marginal ray that meets the tip of the CPM is scattered into the system, the effective NA is dependent on the CPM diameter rather than the degree of scattering, and hence effective NA becomes simply $D/2d_1$. Therefore, to meet the requirement that the NA is determined by Eq. (A1), the CPM size has to fulfill the condition that $D > \gamma$, where γ is

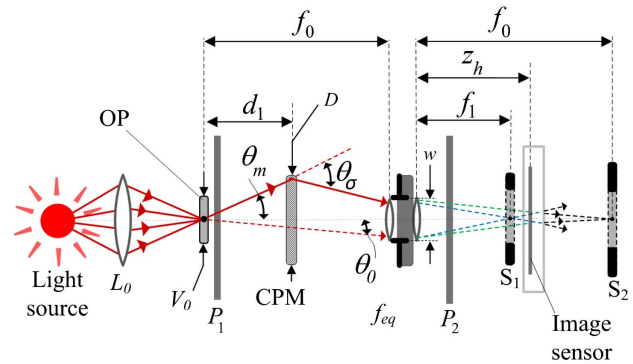$$\gamma = \left[\frac{\lambda \sigma}{\Delta}(f_0 - d_1) + w\right]\frac{d_1}{f_0}. \tag{A3}$$

Fig. 8. Optical schematic of the marginal rays entering the system in the presence of a CPM (the solid red line) and without the CPM (the dashed line).

From the preceding discussion, the trade-off between the gain of the NA Eq. (A2) and the FOV Eq. (9) can be considered. Therefore, the degree of scattering enables the user to choose between the gain of spatial bandwidth and the loss in FOV size.

REFERENCES

1. M. Gu, ed., *Advanced Optical Imaging Theory* (Springer-Verlag, 1999), Vol. **75**.
2. P. Nisenson and C. Papaliolios, "Detection of Earth-like planets using apodized telescopes," Astrophys. J. **548**, L201–L205 (2001).
3. R. Carriles, D. N. Schafer, K. E. Sheetz, J. J. Field, R. Cisek, V. Barzda, A. W. Sylvester, and J. A. Squier, "Invited review article: imaging techniques for harmonic and multiphoton absorption fluorescence microscopy," Rev. Sci. Instrum. **80**, 081101 (2009).
4. A. R. Kherlopian, T. Song, Q. Duan, M. A. Neimark, M. J. Po, J. K. Gohagan, and A. F. Laine, "A review of imaging techniques for systems biology," BMC Syst. Biol. **2**, 74 (2008).
5. E. Hecht, *Optics* (Pearson Education, 2002).
6. B. O. Leung and K. C. Chou, "Review of super-resolution fluorescence microscopy for biology," Appl. Spectrosc. **65**, 967–980 (2011).
7. E. Betzig and J. K. Trautman, "Near-field optics: microscopy, spectroscopy, and surface modification beyond the diffraction limit," Science **257**, 189–195 (1992).
8. M. J. Rust, M. Bates, and X. Zhuang, "Sub-diffraction-limit imaging by stochastic optical reconstruction microscopy (STORM)," Nat. Methods **3**, 793–796 (2006).
9. M. G. L. Gustafsson, "Surpassing the lateral resolution limit by a factor of two using structured illumination microscopy," J. Microsc. **198**, 82–87 (2000).
10. J. R. Hassig, "Digital off-axis holography with synthetic aperture," Opt. Lett. **27**, 2179–2181 (2002).
11. V. Mico, Z. Zalevsky, P. Garcia-Martinez, and J. Garcia, "Single step superresolution by interferometric imaging," Opt. Express **12**, 2589–2596 (2004).
12. G. Indebetouw, Y. Tada, J. Rosen, and G. Brooker, "Scanning holographic microscopy with resolution exceeding the Rayleigh limit of the objective by superposition of off-axis holograms," Appl. Opt. **46**, 993–1000 (2007).
13. Y. Kashter and J. Rosen, "Enhanced-resolution using modified configuration of Fresnel incoherent holographic recorder with synthetic aperture," Opt. Express **22**, 20551–20565 (2014).
14. J. W. Goodman, *Introduction to Fourier Optics* (McGraw-Hill, 1968).
15. J. Rosen and G. Brooker, "Digital spatially incoherent Fresnel holography," Opt. Lett. **32**, 912–914 (2007).
16. J. Rosen and G. Brooker, "Non-scanning motionless fluorescence three-dimensional holographic microscopy," Nat. Photonics **2**, 190–195 (2008).
17. J. Rosen, N. Siegel, and G. Brooker, "Theoretical and experimental demonstration of resolution beyond the Rayleigh limit by FINCH fluorescence microscopic imaging," Opt. Express **19**, 26249–26268 (2011).
18. J. Rosen and R. Kelner, "Modified Lagrange invariants and their role in determining transverse and axial imaging resolutions of self-interference incoherent holographic systems," Opt. Express **22**, 29048–29066 (2014).
19. Y. Kashter, A. Vijayakumar, Y. Miyamoto, and J. Rosen, "Enhanced super resolution using Fresnel incoherent correlation holography with structured illumination," Opt. Lett. **41**, 1558–1561 (2016).
20. A. Vijayakumar, Y. Kashter, R. Kelner, and J. Rosen, "Coded aperture correlation holography–a new type of incoherent digital holograms," Opt. Express **24**, 12430–12441 (2016).
21. M. K. Kim, "Adaptive optics by incoherent digital holography," Opt. Lett. **37**, 2694–2696 (2012).
22. M. K. Kim, "Incoherent digital holographic adaptive optics," Appl. Opt. **52**, A117–A130 (2013).
23. Y. Choi, T. D. Yang, C. Fang-Yen, P. Kang, K. J. Lee, R. R. Dasari, M. S. Feld, and W. Choi, "Overcoming the diffraction limit using multiple light scattering in a highly disordered medium," Phys. Rev. Lett. **107**, 023902 (2011).
24. Y. Choi, C. Yoon, M. Kim, W. Choi, and W. Choi, "Optical imaging with the use of a scattering lens," IEEE J. Sel. Top. Quantum Electron. **20**, 61–73 (2014).
25. D. J. Goldstein, *Understanding the Light Microscope: A Computer Aided Introduction* (Academic, 1999) Chap. 1.
26. R. W. Gerchberg and W. O. Saxton, "A practical algorithm for the determination of phase from image and diffraction plane pictures," Optik **35**, 227–246 (1972).
27. B. Katz, J. Rosen, R. Kelner, and G. Brooker, "Enhanced resolution and throughput of Fresnel incoherent correlation holography (FINCH) using dual diffractive lenses on a spatial light modulator (SLM)," Opt. Express **20**, 9109–9121 (2012).
28. A. Vijayakumar, Y. Kashter, R. Kelner, and J. Rosen, "Coded aperture correlation holography (COACH) system with improved performance," Appl. Opt. **56**, F67–F77 (2017).